

The Challenges of the Nonlinear Regime for Physics-Informed Neural Networks

Andrea Bonfanti^{1,2,3} Giuseppe Bruno¹ Cristina Cipriani^{4,5,6}

Abstract

The Neural Tangent Kernel (NTK) viewpoint represents a valuable approach to examine the training dynamics of Physics-Informed Neural Networks (PINNs) in the infinite width limit. We leverage this perspective and focus on the case of nonlinear Partial Differential Equations (PDEs) solved by PINNs. We provide theoretical results on the different behaviors of the NTK depending on the linearity of the differential operator. Moreover, inspired by our theoretical results, we emphasize the advantage of employing second-order methods for training PINNs. Additionally, we explore the convergence capabilities of second-order methods and address the challenges of spectral bias and slow convergence. Every theoretical result is supported by numerical examples with both linear and nonlinear PDEs, and we validate our training method on benchmark test cases.

1. Introduction

PINNs became ubiquitous in the scientific research community as a meshless and practical alternative tool for solving PDEs. The first attempts to exploit machine learning models for PDE solutions can be traced back to two articles from the 90s (Dissanayake & Phan-Thien, 1994; Lagaris et al., 1998), while the model acquired its name and popularity through a later publication (Raissi et al., 2019).

Due to the flexible structure of the architecture, PINNs can be used for forward and inverse problems (Yang et al., 2021) and efficiently exploited for more complex engineering practice such as constrained shape and topology optimization, and surrogate modeling (Sun et al., 2022; Jeong et al., 2023).

However, the usability of PINNs for such use cases is often hindered by their training, which can be very slow and, in some scenarios, not converging to an admissible solution. Due to the black-box nature of PINNs, it is in practice difficult to study their training process and convergence properties from a mathematical perspective (Krishnapriyan et al., 2021). Nonetheless, training speed and convergence are two crucial aspects of any PDE solver that aims to be used in engineering applications.

In those terms, the most interesting results have mainly been obtained through the lenses of the Neural Tangent Kernel (Jacot et al., 2018) for linear PDEs. This perspective has proven to be extremely useful as it highlighted various pathologies intrinsic to the training of PINNs. The most salient being the spectral bias characteristic of Neural Networks (Wang et al., 2021b; Deshpande et al., 2022; Rahaman et al., 2019); the complexity of the loss landscape generated by the PDE residuals (Krishnapriyan et al., 2021); and a crucial interplay between the components of the loss function (Wang et al., 2021a).

In this paper, our objective is to leverage the NTK perspective for analyzing the challenges of the training and the convergence dynamics of PINNs. Specifically:

- We showcase the significant theoretical distinctions between the usage of PINNs for solving linear PDEs compared to their nonlinear counterparts, outlining the differences between their NTK dynamics.
- We motivate the substantial advantages obtained by employing second-order optimizers for training PINNs, particularly in the nonlinear case.
- We substantiate our theoretical insights with numerical examples, validating the implications of our analysis.

Our work is organized as follows: Section 2 introduces PINNs, while Section 3 provides the fundamentals of NTK theory applied to PINNs. In this section, we conduct a comparative theoretical analysis of NTK behavior in both linear and nonlinear cases. Each theoretical proposition is substantiated by corresponding numerical examples. In Section 4, we discuss convergence guarantees in the aforementioned scenarios, distinguishing between first-order and second-order optimization methods. Finally, Section 5 displays our numerical experiments.

¹BMW Group, Digital Campus Munich (DCM), Munich, Germany ²University of the Basque Country (UPV/EHU), San Sebastian-Donostia, Spain ³Basque Center for Applied Mathematics (BCAM), Bilbao, Spain ⁴Technical University Munich (TUM), Department of Mathematics, Munich, Germany ⁵Munich Center for Machine Learning (MCML), Munich, Germany ⁶Munich Data Science Institute (MDSI), Munich, Germany. Correspondence to: Andrea Bonfanti <Andrea.BA.Bonfanti@bmw.de>, Giuseppe Bruno <Giuseppe.GB.Bruno@bmw.de>, Cristina Cipriani <crisrina.cipriani@ma.tum.de>.

2. Physics-Informed Neural Networks

We address the following PDE formulated on a bounded domain $\Omega \subset \mathbb{R}^{d_{\text{in}}}$,

$$\begin{aligned} \mathcal{R}u(x) &= f(x), & x \in \Omega, \\ u(x) &= g(x), & x \in \partial\Omega, \end{aligned} \quad (1)$$

Here, the PDE is defined with respect to the differential operator \mathcal{R} , while the boundary and initial conditions are collected in the function g .

PINNs aim to approximate the PDE solution $u : \Omega \rightarrow \mathbb{R}^{d_{\text{out}}}$ with a neural network $u_\theta : \Omega$ parametrized by θ , which is a vector containing all the parameters of the network. The ‘‘Physics-Informed’’ nature of the neural network u_θ lies in the choice of the loss function employed during training:

$$\begin{aligned} \mathcal{L}(\theta) &= \frac{1}{2} \int_{\Omega} |\mathcal{R}u(x) - f(x)|^2 dx \\ &+ \frac{1}{2} \int_{\partial\Omega} |u(x) - g(x)|^2 d\sigma(x). \end{aligned} \quad (2)$$

In this work, we specifically focus on scenarios where the PDE involves a nonlinear differential operator. Moreover, without loss of generality we consider the case where the function $f(x) = 0$. Since the function $f(x)$ does not depend on the parametrization, all of our results hold also for the case when it is nonzero. Consequently, we express (1) as

$$\begin{aligned} R(\Phi[u](x)) &= 0, & x \in \Omega, \\ u(x) &= g(x), & x \in \partial\Omega, \end{aligned} \quad (3)$$

where $\Phi[u] : \mathbb{R}^{d_{\text{in}}} \rightarrow \mathbb{R}^{k \times d_{\text{out}}}$, defined as

$$\Phi[u](x) = [u(x), \partial_x u(x), \partial_x^2 u(x), \dots, \partial_x^k u(x)] \quad (4)$$

denotes a vector encompassing all (possibly mixed) derivatives of u until order k , while $R : \mathbb{R}^{k \times d_{\text{out}}} \rightarrow \mathbb{R}$ represents a differentiable function of the components of $\Phi[u]$.

Remark 2.1. The importance of the function R lies in its ability to completely encode the nonlinearity of the PDE, while the term Φ remains linear. Furthermore, for numerous well-known nonlinear PDEs (such as Burger or Navier-Stokes equations), the function R exhibits a distinctive structure as it takes the form of a second-order polynomial.

To illustrate this, we consider the example of the inviscid Burger equation, which for $(\tau, x) \in \Omega$ is expressed as

$$\partial_\tau u + u \partial_x u = 0,$$

This leads to the following representations:

$$\begin{aligned} \Phi[u](\tau, x) &= [u(\tau, x), \partial_\tau u(\tau, x), \partial_x u(\tau, x)], \\ R(z_1, z_2, z_3) &= z_2 + z_1 z_3. \end{aligned}$$

3. Neural Tangent Kernel for PINNs

We now introduce and develop the NTK for PINNs, inspired by the definition in (Wang et al., 2022). We employ a fully-connected neural network featuring a single hidden layer and the standard NTK rescaling: for any $x \in \mathbb{R}^{d_{\text{in}}}$,

$$u_\theta(x) := \frac{1}{\sqrt{m}} W^1 \cdot \sigma(W^0 x + b^0) + b^1. \quad (5)$$

Here, $W^0 \in \mathbb{R}^{m \times d_{\text{in}}}$ and $b^0 \in \mathbb{R}^m$ denote the weights matrix and bias vector of the hidden layer, while $W^1 \in \mathbb{R}^{d_{\text{out}} \times m}$ and $b^1 \in \mathbb{R}^{d_{\text{out}}}$ are the corresponding parameters of the outer layer. For brevity, we denote with θ the collection of all the trainable parameters of the network, i.e. W^1, W^0, b^1, b^0 . Additionally, $\sigma : \mathbb{R} \rightarrow \mathbb{R}$ is a smooth coordinate-wise activation function, such as the hyperbolic tangent, which is a common choice for PINNs.

Furthermore, we adopt the NTK rescaling $\frac{1}{\sqrt{m}}$ to adhere to the methodology introduced in the original work (Jacot et al., 2018). This is crucial for achieving a consistent asymptotic behavior of neural networks as the width of the hidden layer approaches infinity.

Remark 3.1. For the sake of brevity, we focus on the case of neural networks with a single hidden layer. However, most of the outcomes derived in this scenario can be extended to deep networks. We leave this extension to future works.

Moreover, we consider the discrete loss on the collocation points $x_i^r \in \Omega$ and the boundary points $x_i^b \in \partial\Omega$,

$$L(\theta) = \frac{1}{2N_r} \sum_{i=1}^{N_r} |r_\theta(x_i^r)|^2 + \frac{1}{2N_b} \sum_{i=1}^{N_b} |u_\theta(x_i^b) - g(x_i^b)|^2, \quad (6)$$

where $r_\theta(x_i^r) = R(\Phi[u_\theta](x_i^r))$ indicates the residual term. Furthermore, N_r and N_b denote the batch size of, respectively, the collection of $\mathbf{x}^r = \{x_i^r\}_{i=1}^{N_r}$ and $\mathbf{x}^b = \{x_i^b\}_{i=1}^{N_b}$, which are the discrete data used for training. We now consider the minimization of (6) as the gradient flow

$$\partial_t \theta(t) = -\nabla L(\theta(t)). \quad (7)$$

Using the following notation

$$\begin{aligned} u_\theta(\mathbf{x}^b) &= \{u_{\theta(t)}(x_i^b)\}_{i=1}^{N_b}, \\ r_\theta(\mathbf{x}^r) &= \{r_{\theta(t)}(x_i^r)\}_{i=1}^{N_r}, \end{aligned} \quad (8)$$

we can characterize how these quantities evolve during the gradient flow, through the NTK perspective.

Lemma 3.2. *Given the data points (8) and the gradient flow (7), then u_θ and r_θ satisfy the following evolution*

$$\begin{bmatrix} \partial_t u_{\theta(t)}(\mathbf{x}^b) \\ \partial_t r_{\theta(t)}(\mathbf{x}^r) \end{bmatrix} = -K(t) \begin{bmatrix} u_{\theta(t)}(\mathbf{x}^b) - g(\mathbf{x}^b) \\ r_{\theta(t)}(\mathbf{x}^r) \end{bmatrix} \quad (9)$$

where $K(t) = J(t)J(t)^T$ and

$$J(t) = \begin{bmatrix} \partial_{\theta} u_{\theta(t)}(\mathbf{x}^b) \\ \partial_{\theta} r_{\theta(t)}(\mathbf{x}^r) \end{bmatrix}. \quad (10)$$

Proof. The proof is presented in (Wang et al., 2022). \square

We provide more details about the construction of $J(t)$ in Appendix A. The matrix K is also referred to as Gram matrix. The analysis of Gram matrices and their behavior in the infinite width limit (Du & Lee, 2018; Du et al., 2019) yields results akin to the NTK analysis.

It is important to note that this definition is applicable to any type of sufficiently regular differential operator. In the subsequent discussion, we compare the behavior of the kernel during training based on the characteristics of the differential operator.

3.1. Linear PDEs

In the work by (Wang et al., 2022), PINNs have been thoroughly investigated using the NTK, with a particular emphasis on the case of linear PDEs. Additionally, the work by (Liu et al., 2020) extensively explored the case of standard neural networks with linear output. Here, we present their findings to establish a basis for comparison with the nonlinear case, which is the primary focus of our investigation.

First of all, we list here all the assumptions needed on the differential operator \mathcal{R} and the neural network in (5).

Assumption 3.3 (on \mathcal{R}). The differential operator \mathcal{R} is linear, which implies that R is linear.

Assumption 3.4 (on the network). Given the network (5), we assume the following properties:

- (i) there exists a constant $C > 0$ such that all parameters of the network are uniformly bounded for $t \in [0, T]$,

$$\sup_{t \in [0, T]} \|\theta(t)\|_{\infty} \leq C \quad \text{with } C \text{ independent from } m.$$

- (ii) there exists a constant $C > 0$ such that

$$\int_0^T \left| \sum_{i=1}^{N_b} (u_{\theta(\tau)}(x_i^b) - g(x_i^b)) \right| d\tau \leq C,$$

$$\int_0^T \left| \sum_{i=1}^{N_r} (\Phi[u_{\theta(\tau)}](x_i^r)) \right| d\tau \leq C.$$

- (iii) the activation function σ and as well as its derivatives $\sigma^{(i)}$ up to power $k + 1$ are smooth and $|\sigma^{(i)}| \leq C$ for $i = 1, \dots, k$, where $\sigma^{(i)}$ denotes the i -th order derivative of σ .

In order to present the results, we denote with H_r the Hessian of the residuals r_{θ} with respect to the parameters θ . The Hessian plays an important role in Proposition 3.5, which aims to list all the prior results that can be derived by combining Theorem 4.4 of (Wang et al., 2022), Theorem 3.2 of (Liu et al., 2020).

Proposition 3.5. Consider a fully-connected neural network given by (5), under the Assumption 3.4 on the network and Assumption 3.3 on the PDE. For the minimization of the loss function (6) through gradient flow, starting from a Gaussian random initialization $\theta(0)$, it holds that for any $T > 0$,

- the randomly initialized tangent kernel $K(0)$ converges in probability to a deterministic kernel \bar{K} as $m \rightarrow \infty$;
- the Hessian matrix H_r of the residuals is sparse and

$$\|H_r\| = O\left(\frac{1}{\sqrt{m}}\right),$$

hence the spectral norm converges to 0 as $m \rightarrow \infty$;

- as a consequence, the NTK is nearly constant during training, i.e.

$$\lim_{m \rightarrow \infty} \sup_{t \in [0, T]} \|K(t) - K(0)\|_2 = 0;$$

Proof. The proof can be found in the papers mentioned above or as a special (linear) case in Appendix B-D. \square

As noted in (Liu et al., 2020), the constancy of the neural tangent kernel during training is equivalent to the linearity of the model. This characteristic is related to the vanishing of the (norm of the) Hessian of the loss in the infinite width limit. However, in the following section, we show that this is not the case when the PDE is nonlinear.

3.2. Nonlinear PDEs

We present our findings in the case of nonlinear PDEs, and draw comparisons with Proposition 3.5. While the network and its assumptions remain the same, we now specify the assumptions pertaining to the nonlinear PDE.

Assumption 3.6 (on \mathcal{R}). The differential operator \mathcal{R} is nonlinear, hence the function R is nonlinear. Moreover, the gradient ∇R is continuous.

The first distinction arises in the convergence of the NTK at initialization in the infinite width limit.

Theorem 3.7. Consider a fully-connected neural network given by (5) satisfying Assumption 3.4. Moreover, the PDE satisfies Assumption 3.6. Then, under a Gaussian random initialization $\theta(0)$, it holds that,

$$K(0) \xrightarrow{D} \bar{K} \quad \text{as } m \rightarrow \infty,$$

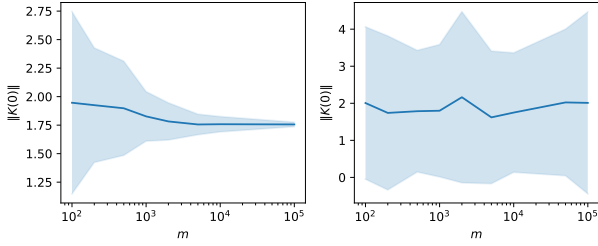


Figure 1. Mean and standard deviation of the spectral norm of $K(0)$ as a function of the number of neurons m for 10 independent experiments. Left: linear case. Right: nonlinear case.

where the limit is in distribution and \bar{K} is not deterministic, but its law can be explicitly characterized.

Proof. The details of the proof are presented in Appendix B. However, the intuition behind the proof is to rewrite the kernel at initialization as

$$K(0) = \Lambda_R(0) K_\Phi(0) \Lambda_R(0)^T,$$

where the matrix $K_\Phi(0)$ enclose the linear components of \mathcal{R} , hence the derivatives of the network's output, while the matrix $\Lambda_R(0)$ depends on the gradient of R (so its contribution is relevant just in the nonlinear case). We can establish the convergence in probability of $K_\Phi(0)$ to a deterministic matrix by taking advantage of the linearity of the operator Φ and commuting Φ and ∂_θ (see Lemma B.2). The matrix $\Lambda_R(0)$ only converges in distribution, since it is a function of the network output and its derivatives, whose limits are a Gaussian Process at initialization by Proposition B.1. \square

This result is confirmed by the numerical experiments depicted in Figure 1. In the linear case the initialization converges to some constant when $m \rightarrow \infty$, while this does not happen in the nonlinear case.

Remark 3.8. It is worth mentioning that \bar{K} does not align with the typical definition of a kernel, due to its stochastic nature. From a mathematical perspective it is more correct to refer to it as a stochastic Gram matrix. However, with an abuse of notation, we refer to it as NTK for continuity.

Next, we focus on the NTK behavior during training.

Proposition 3.9. *Under Assumption 3.4 on the network, and Assumption 3.6 on the PDE, assume additionally that R is a real analytic function. Let u_* be a solution of the corresponding PDE and suppose that for every $m \in \mathbb{N}$ there exists t_m such that*

$$\|u_\theta(t_m) - u_*\|_{C^k} \leq \varepsilon_m, \text{ with } \varepsilon_m \rightarrow 0 \text{ as } m \rightarrow \infty. \quad (11)$$

Finally, let $\theta(t)$ be obtained through gradient flow as defined in (7) and denote by $K(t)$ the corresponding NTK. For

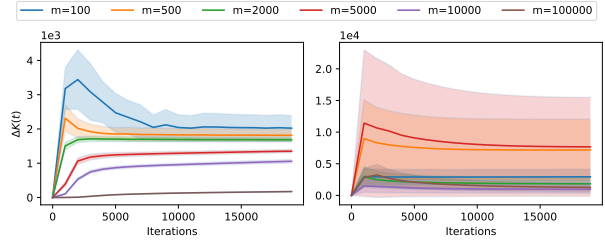


Figure 2. Mean and standard deviation of $\Delta K(t) := \frac{\|K(t) - K(0)\|}{\|K(0)\|}$ over the network's width m , for 10 independent experiments. Left: linear case. Right: nonlinear case.

$\theta(0) \sim \mathcal{N}(0, I_m)$, the following holds:

$$\lim_{m \rightarrow \infty} \sup_{t \in [0, T]} \|K(t) - K(0)\| > 0 \text{ a.s.}$$

Proof. The proof can be found in Appendix C. \square

Remark 3.10. It's important to note that our result holds under the assumption that a neural network with $m \rightarrow \infty$ can effectively approximate the solution u^* of the PDE (1) and the training is successful to do so. The first assumption is reasonable, given results such as the universal approximation theorem for neural networks (Cybenko, 1989). Proposition 3.9 shows that, even in this optimistic training scenario, the constancy of the kernel is not possible.

The statement of Proposition 3.9 is confirmed by the numerical experiments depicted in Figure 2, which illustrates the contrast between the linear and nonlinear cases. Unlike the linear case, the constancy of the NTK during training is not attainable in the nonlinear case.

Essentially, in the context of nonlinear PINNs, achieving convergence to a linear regime is not feasible. The reason behind this phenomenon is related to the spectral norm of H_r . The fact that the latter converges to 0 as $m \rightarrow \infty$ is fundamental for the proof of Proposition 3.5. This is what allows the transition to a linear regime, as shown in (Liu et al., 2020) for different deep learning architectures. However, this is not the case for nonlinear PDEs.

Proposition 3.11. *Under Assumption 3.4 on the network and Assumption 3.6 on the PDE, let us further assume that R is a second-order polynomial. Then, the Hessian of the residuals H_r is not sparse and*

$$\lim_{m \rightarrow \infty} \|H_r\| \geq \tilde{c},$$

where the constant \tilde{c} does not depend on m .

Proof. The proof can be found in Appendix C, together with an explicit formula for \tilde{c} . \square

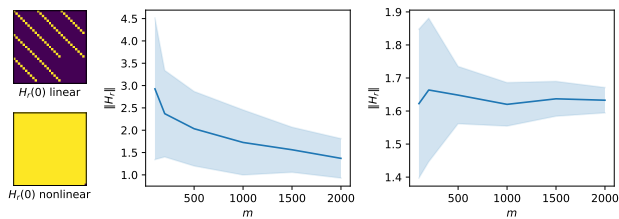


Figure 3. Left: in yellow the non-zero components of the Hessian matrix at initialization (up in the linear case, down the nonlinear one). Center: mean and standard deviation of the spectral norm of the $H_r(0)$ over m in the linear case (for 10 independent experiments). Right: same as Center, but for a nonlinear PDE.

Remark 3.12. For the latter result, we introduce the additional requirement that R is a second-order polynomial. This assumption encompasses many well-known nonlinear PDEs (e.g. Burger or Navier-Stokes equations).

This result is supported by Figure 3, where we compare the sparsity of the Hessian at initialization $H_r(0)$ in both the linear and nonlinear case. Moreover, we observe that in the linear scenario $\|H_r\|$ decays as m grows, contrarily to the nonlinear example, as expected.

4. Convergence results

Traditional analyses of the gradient descent (7) often rely on the smoothness or even convexity of the loss, assumptions that may not hold in the context of deep learning. As an alternative, numerous results concentrate on the infinite width limit, particularly in connection with the NTK analysis. While we refrain from presenting a formal proof, as it has been extensively addressed in existing literature, we highlight the notable result below.

Theorem 4.1. *Under Assumption 3.3 on the PDE and Assumption 3.4 on the network defined by (5), consider the scenario where m is sufficiently large. With high probability on the random initialization, there exists a constant $\mu > 0$, depending on the eigenvalues of K , such that gradient descent, employing a sufficiently small step size η , converges to a global minimizer of (6) with an exponential convergence rate, i.e.*

$$L(\theta(t)) \leq (1 - \eta\mu)^t L(\theta(0)).$$

Proof. See (Gao et al., 2023), (Du & Lee, 2018), (Liu et al., 2020), and others. \square

It is noteworthy that this result is presented at the level of gradient descent, i.e. the discretization of the gradient flow (7), which explains the constant η representing its step size. This convergence theorem has also been extended to various types of architectures in (Du et al., 2019).

We emphasize that the convergence result in Theorem 4.1 is rooted in the applicability of the Polyak-Lojasiewicz condition which, in turn, is linked to the smallest eigenvalue of the tangent kernel (as μ). In the case of linear networks, the tangent kernel $K(t)$ is positive definite (Gao et al., 2023) for any $t \in [0, T]$, leading to positive eigenvalues. The key finding in this context is that if m is sufficiently large, $K(t) \approx \bar{K}$, where \bar{K} is the deterministic matrix of Proposition 3.5, which only depends on the training input and not on the network’s parameters θ . As a result, in the infinite width regime, the dynamics (9) can be approximated by

$$\begin{bmatrix} \partial_t u_\theta(x^b) \\ \partial_t r_\theta(x^r) \end{bmatrix} = -\bar{K} \begin{bmatrix} u_\theta(x^b) - g(x^b) \\ r_\theta(x^r) \end{bmatrix}.$$

Importantly, this necessitates not only the positive definiteness of the kernel $K(0)$ at initialization but also the persistence of positive eigenvalues throughout training. In the linear case, this follows from the nearly constancy of the NTK.

Remark 4.2. In the case of nonlinear networks, demonstrating the persistence of positive definiteness of the kernel becomes challenging. First of all, the matrix has some stochastic components, so its positive definiteness can only be showed in probability. Moreover, even at initialization the same reasoning as (Gao et al., 2023) or (Du & Lee, 2018) does not apply in this case and it is not possible to show that the eigenvalues of $K(0)$ in the nonlinear case are all positive. Nevertheless, we believe that this question warrants further investigation, potentially utilizing tools from random matrix theory to bound the smallest singular value of K .

In practice, PINNs exhibit the phenomenon recognized as *spectral bias* (Wang et al., 2021b; Deshpande et al., 2022; Rahaman et al., 2019). Notably, it is observable that the eigenvalues of the NTK of PINNs decay rapidly. As the eigenvalues of the tangent kernel characterize the rate at which the training error diminishes, the presence of small or unbalanced eigenvalues leads to slow convergence, particularly for high-frequency components of the loss function, or even failure in training. This happens regardless of the linearity of the differential operator \mathcal{R} of the PDE.

Because of all the aforementioned reasons, our focus turns to the investigation of the behavior of second-order optimization methods.

4.1. Second-Order Optimization Methods

Second-order optimization methods are powerful algorithms that leverage both the gradient and the Hessian of the loss function. Within this category, Quasi-Newton methods stand out as the most natural, relying on the Newton update rule

$$\theta(t+1) = \theta(t) - [\nabla^2 L(\theta(t))]^{-1} \nabla L(\theta(t)). \quad (12)$$

However, the application of this update step relies on second-order derivatives, which are prohibitively expensive to compute as the number of parameters in the model increases. Indeed, the core idea behind Quasi-Newton methods involves utilizing an approximation of the Hessian such as the one of the Gauss-Newton method

$$\nabla^2 L(\theta) = J^T(t)J(t) + H_r r_{\theta(t)} \approx J^T(t)J(t) \quad (13)$$

in the formula (12). Here, $J(t) \in \mathbb{R}^{n \times p}$ represents the Jacobian of the loss at the training time t , and it aligns with the definition in (10). As the Jacobian $J(t)$ is already calculated when evaluating the gradient, the approximation (13) does not necessitate additional derivative evaluations, resulting in significant computational time savings.

We now tackle the issues of spectral bias and slow convergence by presenting a result applicable to the Gauss-Newton method. In practice, when the number of parameters p is larger than number of samples n , the matrix $J^T(t)J(t)$ is surely singular. In this case, we consider the generalized inverse $(J^T(t)J(t))^\dagger$, instead of the inverse.

Theorem 4.3. *Consider the parameter $\theta(t)$ obtained by the Gauss-Newton flow below*

$$\partial_t \theta(t) = -(J^T(t)J(t))^\dagger \nabla L(\theta(t)). \quad (14)$$

Then, the following holds

$$\begin{bmatrix} \partial_t u_{\theta(t)}(\mathbf{x}^b) \\ \partial_t r_{\theta(t)}(\mathbf{x}^r) \end{bmatrix} = -U(t)D(t)U(t)^T \begin{bmatrix} u_{\theta(t)}(\mathbf{x}^b) \\ r_{\theta(t)}(\mathbf{x}^r) \end{bmatrix}, \quad (15)$$

where $U(t) \in \mathbb{R}^{n \times n}$ is a unitary matrix and $D \in \mathbb{R}^{n \times p}$ is a diagonal matrix with entries 0 or 1. In particular, if $J(t)$ is full-rank for any $t \in [0, T]$, then convergence to a global minimum is attained.

Proof. The proof is presented in Appendix E. \square

In the nonlinear case, the established results (Gao et al., 2023) demonstrating the convergence of gradient descent to global minima fall short, even under the full-rank assumption. This limitation arises due to the requirement of a uniform (across training time) bound on the smallest eigenvalue of the NTK, typically achieved by exploiting the constancy of the NTK in the infinite width limit. However, as demonstrated in Proposition 3.9, the constancy property does not hold in the nonlinear case.

Remark 4.4. Even without the full-rank assumption, Theorem 4.3 highlights another advantage of second-order methods: the training is nearly spectrally unbiased, since the nonzero eigenvalues of the ODE’s controlling matrix in (15) become 1.

We refer to the numerical results presented in Figure 4 for a comparison of the eigenvalues when training with first-order or second-order methods.

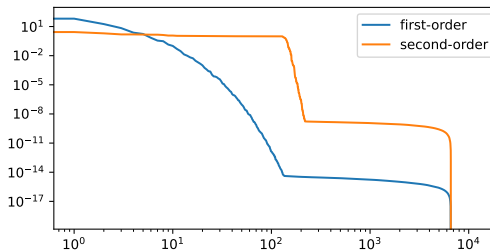


Figure 4. Eigenvalues of $K(0)$ for a first-order optimizer and $D(0)$ for a second-order method applied to Burger equation.

5. Numerical Experiments

Training Algorithm Among all the second-order methods, in our numerical experiments we make use of a modified version of the Levenberg-Marquardt (LM) algorithm, as it offers further stability through the update rule

$$\theta(t+1) = \theta(t) - [J^T(t)J(t) + \lambda \text{Id}_p]^{-1} \nabla L(\theta(t)),$$

where λ is a damping parameter adjusted by the algorithm.

In practice, the iterative step of the LM can be considered as an average, weighted by λ , between the Gradient Descent step and a Gauss-Newton method.

This aspect of the LM represents its crucial advantage over other Quasi-Newton methods such as Gauss-Newton or BFGS. Indeed, Quasi-Newton methods show good performance when the initial guess of the solution u_θ is close to the correct one. The update rule of LM avoids this issue by relying on simil-gradient descent steps at early iteration. Moreover, the parameter λ typically decreases during training, in order to converge to a Quasi-Newton method when close to the optimum.

Moreover, another recommended enhancement is given by the geodesic acceleration proposed in (Fletcher, 1971). Its main advantage is to speed up convergence when the optimizer must move through a loss landscape which presents very steep valleys, which is the case of PINNs (Krishnapriyan et al., 2021). For the details on the implementation of the modified LM algorithm used in this work, along with its pseudocode, please refer to Appendix F. In the following, we describe the numerical experiments.

Details on the Networks The neural network architectures adopted in the experiments are standard Vanilla PINNs with hyperbolic tangent as activation function. All of the PINNs trained in our analysis are characterized by 5 hidden layers with 20 neurons each. Every training is performed for 10 independent neural networks with weights initialized with Xavier normal distribution (Glorot et al., 2011). All models are implemented in PyTorch (Paszke et al., 2019),

the training is stopped after one hour of computation on a single NVIDIA T4 GPU.

Test Cases We assess our theoretical findings on the following equations:

- *Wave/Poisson Equation*: despite being linear PDEs, they represent a suitable scenario to showcase the detrimental effect of the spectral bias on the training of PINNs, due to the presence of high-frequency components in the solution.
- *Burger Equation*: this is ubiquitous as a nonlinear PDE for testing PINN-based models. Being a relatively simple PDE, a PINN can typically reach a valid solution, even with a first-order optimizer.
- *Navier-Stokes Equation*: this is a very challenging equation for both PINNs and classical methods. It is a non-linear PDE, recurrent in applications. We test the case of the flow past a cylinder in 2D.

For the sake of compactness, we refer to Appendix F for a detailed description of the specific instances of the aforementioned PDEs..

5.1. Numerical Results

The results obtained by the LM algorithm are compared with those obtained by Adam (Kingma & Ba, 2014) and L-BFGS (Liu & Nocedal, 1989), which are the optimizer typically used to train PINNs.

In Figure 5, we showcase the relative L^2 loss obtained on the test set during training on the Wave equation with the aforementioned optimizers. While Adam and L-BFGS get stuck relatively fast in a local minima, the LM algorithm is able to decrease the loss consistently, despite the complexity of the problem. The poor performance of L-BFGS can be motivated by two factors. On one hand, the Hessian computed during BFGS iterations is merely an approximation of the true Hessian; on the other hand, convergence to the true solution is heavily hindered since the initial guess is typically not close to the correct one.

In Figure 6 and Figure 7, it is possible to notice the effect of the spectral bias: the PINN trained with Adam can capture only the lower frequency components of the true solution, while the model trained with LM performs better as the spectral bias is alleviated in accordance with Theorem 4.3. It is worth noticing that the same holds even when introducing the loss balancing suggested in (Wang et al., 2022): its performance is showed in Figure 7.

A possible concern might be the computational time of first-order method, in comparison with second-order ones, that

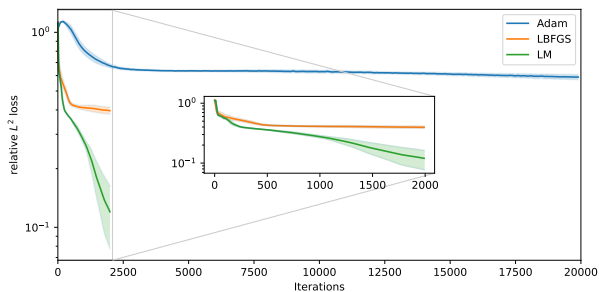


Figure 5. Mean and standard deviation of the relative L^2 loss on the test set on the Wave equation for Adam, L-BFGS and LM optimizer over iterations (repetition over 10 independent runs).

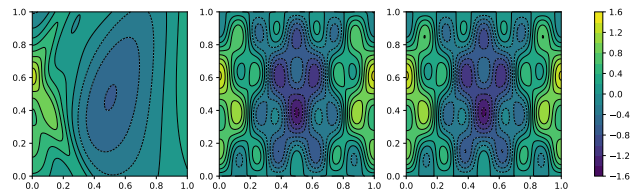


Figure 6. Experiments on the Wave equation. Left: Prediction of the parametrized solution of a PINN trained with Adam (Left) and LM (Center) alongside with the true solution (Right).

is why in Figure 8, we present the relative L^2 loss over the computational time when training on Burger equation. Due to the relatively simplicity of the equation, all the training methods are able to reach a reasonable solution. However, while the precision of PINNs trained with Adam and L-BFGS is around 10^{-3} , the precision of PINNs trained with LM can reach a precision around 10^{-5} . The same behavior can be consistently observed in all of our tests, which attain a precision comparable or even better than the state-of-the-art presented in (Hao et al., 2023; Wang et al., 2021b). Such improvement is crucial since the target of the neural network is the solution of a PDE, which might require arbitrary precision in certain applications.

Finally, in Figure 9 and Figure 10, we show that by employing the LM optimizer, it is possible to obtain a reasonable

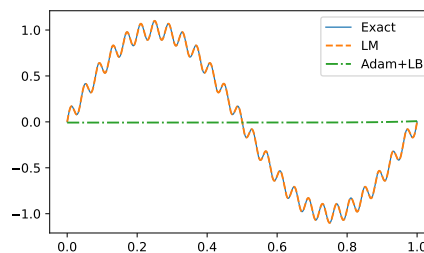


Figure 7. Experiments on the prediction of the solution of Poisson equation with LM and Adam (with loss balancing), both compared with the exact solution.

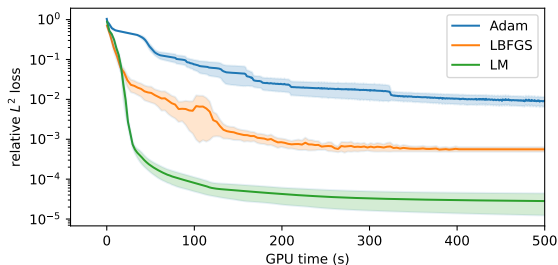


Figure 8. Mean and standard deviation of the relative L^2 loss during training on Burger equation for Adam, L-BFGS and LM optimizers over computational time (repetitions over 10 independent runs).

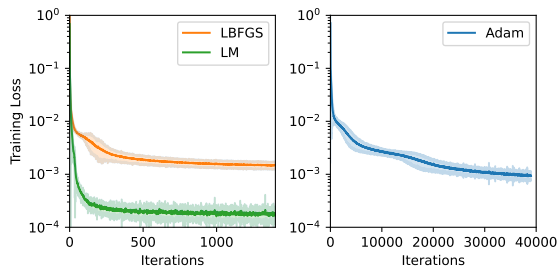


Figure 9. Mean and standard deviation of the training loss over the iterations for Adam, L-BFGS and LM on Navier-Stokes equation (for 10 independent runs).

solution even for a PDE as complex as Navier-Stokes with relatively small architectures. In particular, models trained with LM consistently predict the pressure at short times, which is not provided as initial condition and is essential to converge to the correct solution everywhere.

The most interesting aspect of our results is that convergence is possible without introducing any of the typical training protocols, namely loss balancing, causality training, curriculum training, or random Fourier Features. However, in practice, all these enhancement can be combined with a second-order training method to achieve even better accuracy with short computational times.

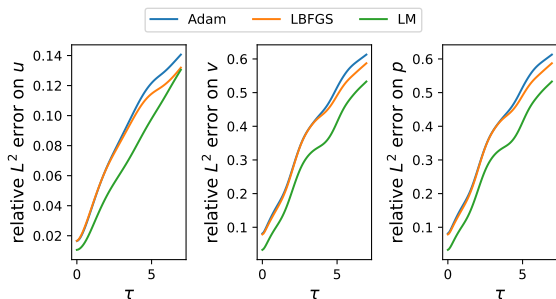


Figure 10. Comparison of the relative L^2 loss over the PDE time τ of Navier-Stokes equation for PINNs trained with Adam, L-BFGS and LM.

5.2. Scalability of the method

An important concern of our findings is related to scalability. Traditionally, second-order methods have been avoided for large machine learning models due to their poor scaling with an increasing number of parameters.

For medium to large-sized networks, the challenge of storing the matrix $J^T J$ in GPU memory becomes infeasible. This can be addressed through an inexact LM method, which involves solving the equivalent system $\|J\theta - r_\theta\| = 0$ using a Krylov subspace iterative method (LQSR or LSMR) (Nocedal & Wright, 1999; Fong & Saunders, 2011). These methods only require Jacobian-vector products, which can be efficiently computed through backpropagation.

Furthermore, there are various strategies for mitigating scalability in the context of PDE solution. In particular, one can resort to methods as domain decomposition or ensemble models like mixture of experts (Gormley & Frühwirth-Schnatter, 2019), in order to allow the usage of relatively small architecture. Interestingly, our experiments demonstrate that even with a relatively small number of parameters, we achieve promising results in solving challenging PDEs.

6. Conclusion

In this paper, we have conducted an in-depth analysis of PINNs training taking advantage of the NTK framework. We have elucidated the distinction that occur in the nonlinear cases in comparison with the linear one and the factors contributing to potential training failures. Additionally, we have delved into the question of convergence. In the linear case, the crucial property of the NTK being positive definite allows for the derivation of gradient flow convergence. However, proving this property in the context of nonlinear networks poses a challenge, and we suggest that techniques from the realm of stochastic Gram matrices could be instrumental in further exploration.

Given that the positive definiteness of the NTK remains a theoretical property even in the case of linear PDEs, we emphasize the significant advantage of employing second-order methods. These optimizers appear to mitigate the spectral bias issue encountered in PINNs. Our theoretical findings have been validated through experiments on various PDEs (both linear and nonlinear), demonstrating that our approach consistently outperforms standard PINNs. Despite our theory being derived in the infinite width limit, our numerical experiments suggest that these conclusions can be effectively applied beyond the overparameterized regime. While we do not claim that other methods do not converge, our results consistently show faster convergence. Future works should tackle the efficiency and scalability of second-order methods, such as LM, in order to enable the applicability to overparameterized deep learning architectures.

References

- Cybenko, G. Approximation by superpositions of a sigmoidal function. *Mathematics of control, signals and systems*, 2(4): 303–314, 1989.
- Deshpande, M., Agarwal, S., and Bhattacharya, A. K. Investigations on convergence behaviour of physics informed neural networks across spectral ranges and derivative orders. In *2022 IEEE Symposium Series on Computational Intelligence (SSCI)*, pp. 1172–1179. IEEE, 2022.
- Dissanayake, M. and Phan-Thien, N. Neural-network-based approximations for solving partial differential equations. *communications in Numerical Methods in Engineering*, 10(3):195–201, 1994.
- Du, S. and Lee, J. On the power of over-parametrization in neural networks with quadratic activation. In *International conference on machine learning*, pp. 1329–1338. PMLR, 2018.
- Du, S., Lee, J., Li, H., Wang, L., and Zhai, X. Gradient descent finds global minima of deep neural networks. In *International conference on machine learning*, pp. 1675–1685. PMLR, 2019.
- Fletcher, R. A modified marquardt subroutine for non-linear least squares. *United Kingdom Atomic Energy Authority Research Group Report*, 1971.
- Fong, D. C.-L. and Saunders, M. Lsmr: An iterative algorithm for sparse least-squares problems. *SIAM Journal on Scientific Computing*, 33(5):2950–2971, 2011.
- Gao, Y., Gu, Y., and Ng, M. Gradient descent finds the global optima of two-layer physics-informed neural networks. In *International Conference on Machine Learning*, pp. 10676–10707. PMLR, 2023.
- Gavin, H. P. The levenberg-marquardt algorithm for nonlinear least squares curve-fitting problems. *Department of civil and environmental engineering, Duke University*, 19, 2019.
- Glorot, X., Bordes, A., and Bengio, Y. Deep sparse rectifier neural networks. In *Proceedings of the fourteenth international conference on artificial intelligence and statistics*, pp. 315–323. JMLR Workshop and Conference Proceedings, 2011.
- Gormley, I. C. and Frühwirth-Schnatter, S. Mixture of experts models. *Handbook of mixture analysis*, pp. 271–307, 2019.
- Hao, Z., Yao, J., Su, C., Su, H., Wang, Z., Lu, F., Xia, Z., Zhang, Y., Liu, S., Lu, L., et al. Pinnacle: A comprehensive benchmark of physics-informed neural networks for solving pdes. *arXiv preprint arXiv:2306.08827*, 2023.
- Jacot, A., Gabriel, F., and Hongler, C. Neural tangent kernel: Convergence and generalization in neural networks. *Advances in neural information processing systems*, 31, 2018.
- Jeong, H., Batuwatta-Gamage, C., Bai, J., Xie, Y. M., Rathnayaka, C., Zhou, Y., and Gu, Y. A complete physics-informed neural network-based framework for structural topology optimization. *Computer Methods in Applied Mechanics and Engineering*, 417:116401, 2023.
- Kingma, D. P. and Ba, J. Adam: A method for stochastic optimization, 2014. URL <https://arxiv.org/abs/1412.6980>.
- Krishnapriyan, A., Gholami, A., Zhe, S., Kirby, R., and Mahoney, M. W. Characterizing possible failure modes in physics-informed neural networks. *Advances in Neural Information Processing Systems*, 34:26548–26560, 2021.
- Lagaris, I. E., Likas, A., and Fotiadis, D. I. Artificial neural networks for solving ordinary and partial differential equations. *IEEE transactions on neural networks*, 9(5):987–1000, 1998.
- Liu, C., Zhu, L., and Belkin, M. On the linearity of large non-linear models: when and why the tangent kernel is constant. *Advances in Neural Information Processing Systems*, 33:15954–15964, 2020.
- Liu, D. C. and Nocedal, J. On the limited memory BFGS method for large scale optimization. *Mathematical programming*, 45(1):503–528, 1989.
- Müller, J. and Zeinhofer, M. Achieving high accuracy with pinns via energy natural gradient descent. In *International Conference on Machine Learning*, pp. 25471–25485. PMLR, 2023.

- Nocedal, J. and Wright, S. J. *Numerical optimization*. Springer, 1999.
- Paszke, A., Gross, S., Massa, F., Lerer, A., Bradbury, J., Chanan, G., Killeen, T., Lin, Z., Gimelshein, N., Antiga, L., et al. Pytorch: An imperative style, high-performance deep learning library. *Advances in neural information processing systems*, 32, 2019.
- Rahaman, N., Baratin, A., Arpit, D., Draxler, F., Lin, M., Hamprecht, F., Bengio, Y., and Courville, A. On the spectral bias of neural networks. In *International Conference on Machine Learning*, pp. 5301–5310. PMLR, 2019.
- Raissi, M. Deep hidden physics models: Deep learning of nonlinear partial differential equations. *The Journal of Machine Learning Research*, 19(1):932–955, 2018.
- Raissi, M., Perdikaris, P., and Karniadakis, G. E. Physics-informed neural networks: A deep learning framework for solving forward and inverse problems involving nonlinear partial differential equations. *Journal of Computational physics*, 378: 686–707, 2019.
- Raissi, M., Yazdani, A., and Karniadakis, G. E. Hidden fluid mechanics: Learning velocity and pressure fields from flow visualizations. *Science*, 367(6481):1026–1030, 2020.
- Sun, Y., Sengupta, U., and Juniper, M. Physics-informed deep learning for simultaneous surrogate modelling and pde-constrained optimization. *Bulletin of the American Physical Society*, 2022.
- Transtrum, M. K. and Sethna, J. P. Improvements to the levenberg-marquardt algorithm for nonlinear least-squares minimization. *arXiv preprint arXiv:1201.5885*, 2012.
- Wang, S., Teng, Y., and Perdikaris, P. Understanding and mitigating gradient flow pathologies in Physics-informed neural networks. *SIAM Journal on Scientific Computing*, 43(5):A3055–A3081, 2021a.
- Wang, S., Wang, H., and Perdikaris, P. On the eigenvector bias of fourier feature networks: From regression to solving multi-scale pdes with physics-informed neural networks. *Computer Methods in Applied Mechanics and Engineering*, 384: 113938, 2021b.
- Wang, S., Yu, X., and Perdikaris, P. When and why PINNs fail to train: A neural tangent kernel perspective. *Journal of Computational Physics*, 449:110768, 2022.
- Yang, L., Meng, X., and Karniadakis, G. E. B-pinns: Bayesian physics-informed neural networks for forward and inverse pde problems with noisy data. *Journal of Computational Physics*, 425:109913, 2021.
- Zhang, G., Martens, J., and Grosse, R. B. Fast convergence of natural gradient descent for over-parameterized neural networks. *Advances in Neural Information Processing Systems*, 32, 2019.

Supplemental Material

This supplemental material is divided into the following six appendices.

- Appendix A: Details about the NTK Matrix
- Appendix B: Proof of Theorem 3.7
- Appendix C: Proof of Proposition 3.9
- Appendix D: Proof of Proposition 3.11
- Appendix E: Proof of Theorem 4.3
- Appendix F: Details about the Numerical Experiments

In the following we denote with $\|\cdot\|_2$ and $\langle \cdot, \cdot \rangle$ the Euclidean and scalar product on \mathbb{R}^d , respectively. The Euclidean ball centered in x with radius R is indicated with $B(x, R)$. We denote with $\|\cdot\|$ the spectral norm of a matrix and with I_n the identity matrix of dimension $n \times n$.

We abbreviate with i.i.d. independently and identically distributed random variables. $\mathbb{E}[X]$ denotes the mean of the random variable $X \in \mathbb{R}^d$, while $\text{Cov}[X]$ is its covariance matrix. Convergence of X_n to X in distribution is indicated with $X_n \xrightarrow{\mathcal{D}} X$, while convergence in probability with $X_n \xrightarrow{\mathcal{P}} X$. \mathcal{GP} denotes a Gaussian Process.

The operator ∇ denotes the gradient of a function on \mathbb{R}^d , while $\partial_x f(x, y)$ the partial derivative of f with respect to the variable x .

A. Details about the NTK Matrix

We define the following matrices

$$\begin{aligned} \partial_\theta u_\theta(x) &= [\partial_{\theta_1} u_\theta(x) \quad \cdots \quad \partial_{\theta_m} u_\theta(x)], \\ \partial_\theta r_\theta(x) &= [\partial_{\theta_1} r_\theta(x) \quad \cdots \quad \partial_{\theta_m} r_\theta(x)], \\ \partial_\theta \Phi[u_\theta](x) &= \begin{bmatrix} \partial_{\theta_1} \Phi_1[u_\theta](x) & \cdots & \partial_{\theta_m} \Phi_1[u_\theta](x) \\ \vdots & \cdots & \vdots \\ \partial_{\theta_1} \Phi_k[u_\theta](x) & \cdots & \partial_{\theta_m} \Phi_k[u_\theta](x) \end{bmatrix}. \end{aligned}$$

By $\partial_\theta u_\theta(\mathbf{x}^b)$, $\partial_\theta r_\theta(\mathbf{x}^r)$ and $\partial_\theta \Phi[u_\theta](\mathbf{x}^r)$ we mean the same matrices as before, calculated in each x_i^b (x_i^r respectively) and stacked vertically, e.g.:

$$\partial_\theta \Phi[u_\theta](\mathbf{x}^b) = \begin{bmatrix} \partial_\theta \Phi[u_\theta](x_1^b) \\ \vdots \\ \partial_\theta \Phi[u_\theta](x_{N_b}^b) \end{bmatrix}.$$

The only exception is given by:

$$\nabla R(\Phi[u_\theta](\mathbf{x}^r)) = \begin{bmatrix} \nabla R(\Phi[u_\theta](x_1^r)) & \mathbf{0} & \cdots & \cdots & \mathbf{0} \\ \mathbf{0} & \nabla R(\Phi[u_\theta](x_2^r)) & \mathbf{0} & \cdots & \mathbf{0} \\ \vdots & \cdots & \cdots & \cdots & \vdots \\ \mathbf{0} & \cdots & \cdots & \mathbf{0} & \nabla R(\Phi[u_\theta](x_{N_r}^r)) \end{bmatrix}. \quad (16)$$

While the Hessians have the following structure:

$$\begin{aligned}
 H_u(x) &:= \begin{bmatrix} \partial_{\theta_1 \theta_1}^2 u_\theta(x) & \cdots & \partial_{\theta_1 \theta_m}^2 u_\theta(x) \\ \vdots & \cdots & \vdots \\ \partial_{\theta_m \theta_1}^2 u_\theta(x) & \cdots & \partial_{\theta_m \theta_m}^2 u_\theta(x) \end{bmatrix}, \\
 H_r(x) &:= \begin{bmatrix} \partial_{\theta_1 \theta_1}^2 r_\theta(x) & \cdots & \partial_{\theta_1 \theta_m}^2 r_\theta(x) \\ \vdots & \cdots & \vdots \\ \partial_{\theta_m \theta_1}^2 r_\theta(x) & \cdots & \partial_{\theta_m \theta_m}^2 r_\theta(x) \end{bmatrix}, \\
 H_{\Phi_i}(x) &:= \begin{bmatrix} \partial_{\theta_1 \theta_1}^2 \Phi_i[u_\theta](x) & \cdots & \partial_{\theta_1 \theta_m}^2 \Phi_i[u_\theta](x) \\ \vdots & \cdots & \vdots \\ \partial_{\theta_m \theta_1}^2 \Phi_i[u_\theta](x) & \cdots & \partial_{\theta_m \theta_m}^2 \Phi_i[u_\theta](x) \end{bmatrix}.
 \end{aligned} \tag{17}$$

B. Proof of Proposition 3.7.

First of all, we derive a result about the behavior of the vector of partial derivatives $\Phi[u]$. The Proposition B.1 below is a generalization of Theorem 4.1 in (Wang et al., 2022) for any derivative of order k . This means that there are no nonlinearities involved, since these are encoded in the function R . Moreover we study the full vector and not each component separately as it is done in (Wang et al., 2022). This is needed in the following proofs.

Proposition B.1. *Consider a fully-connected neural network of one hidden layer as in (5), under Assumption 3.4. Then, starting from $\theta(0)$ i.i.d. from $\mathcal{N}(0, \text{Id})$, it holds that*

$$\Phi[u_{\theta(0)}](x) \xrightarrow{\mathcal{D}} \mathcal{GP}(0, \Sigma(x, x')) \quad \text{for any } x, x' \in \Omega,$$

as $m \rightarrow \infty$, where \mathcal{D} means convergence in distribution and Σ is explicitly calculated.

Proof. To ease the notation, we omit the initial time 0 and denote $u_{\theta(0)}$ with u_θ . Similarly, all the weights matrices and biases $W^1(0), W^0(0), b^1(0), b^0(0)$ are indicated with W^1, W^0, b^1, b^0 . Now according to the definition of Φ and the fact that it is linear, we obtain that

$$\Phi[u_\theta](x) = \frac{1}{\sqrt{m}} W^1 \cdot \Phi[\sigma(W^0 x + b^0)] = \frac{1}{\sqrt{m}} \sum_{j=1}^m W_j^1 \Phi[\sigma(W_j^0 x + b_j^0)].$$

According to our assumptions, $W_j^1 \Phi[\sigma(W_j^0 x + b_j^0)]$ are i.i.d. random variables. We prove below that their moments are finite, hence by the multidimensional Central Limit theorem (CLT) we can conclude that, for every $x \in \Omega$,

$$\Phi[u_\theta](x) \xrightarrow{\mathcal{D}} \mathcal{N}(0, \Gamma(x)),$$

with covariance matrix:

$$\Gamma(x) = \text{Cov}_{u, v \sim \mathcal{N}(0, 1)} [\Phi[\sigma(ux + v)]].$$

Now we compute the covariance of the limit gaussian process. In order to do so, we first need to show that $\Phi_i[u_\theta](x)$ are uniformly integrable with respect to m for every $i = 1, \dots, k$. It follows from:

$$\begin{aligned}
 \sup_m \mathbb{E}[|\Phi_i[u_\theta](x)|^2] &= \sup_m \mathbb{E} \left[\frac{1}{m} \sum_{j, l=1}^m W_j^1 W_l^1 \Phi_i[\sigma(W_j^0 x + b_j^0)] \Phi_i[\sigma(W_l^0 x' + b_l^0)] \right] \\
 &= \sup_m \mathbb{E} \left[\frac{1}{m} \sum_{j=0}^m (W_j^1)^2 \Phi_i[\sigma(W_k^0 x + b_k^0)]^2 \right] = \mathbb{E} [\Phi_i[\sigma(W_j^0 x + b_j^0)]^2] \leq C^2 \tau^2,
 \end{aligned}$$

where $C = \max_{1 \leq i \leq k} \|\sigma^{(i)}\|_\infty$ and $\sigma^{(i)}$ indicates the i -th order derivative of σ , while $\tau = \max_{1 \leq i \leq k} \mathbb{E}_{y \sim \mathcal{N}(0, 1)} [|y|^i] < \infty$.

Now, for any given point $x, x' \in \Omega$ we have that

$$\begin{aligned}
 \Sigma(x, x')_{i,j} &= \lim_{m \rightarrow \infty} \mathbb{E} [\Phi_i[u_\theta](x) \Phi_j[u_\theta](x')] = \\
 &= \lim_{m \rightarrow \infty} \mathbb{E} \left[\frac{1}{m} \sum_{l_1, l_2=1}^m W_{l_1}^1 W_{l_2}^1 \Phi_i[\sigma(W_{l_1}^0 x + b_{l_1}^0)] \Phi_j[\sigma(W_{l_2}^0 x' + b_{l_2}^0)] \right] = \\
 &= \lim_{m \rightarrow \infty} \mathbb{E} \left[\frac{1}{m} \sum_{l=1}^m (W_l^1)^2 \Phi_i[\sigma(W_l^0 x + b_l^0)] \Phi_j[\sigma(W_l^0 x' + b_l^0)] \right] = \\
 &= \mathbb{E}_{u, v \sim \mathcal{N}(0,1)} [\Phi_i[\sigma(ux + v)] \Phi_j[\sigma(ux' + v)]].
 \end{aligned}$$

□

Lemma B.2. Consider a fully-connected neural network of one hidden layer as in (5), under Assumption 3.4. Let us define

$$K_\Phi(0) = \begin{bmatrix} \partial_\theta u_{\theta(0)}(\mathbf{x}^b) \\ \partial_\theta \Phi[u_{\theta(0)}](\mathbf{x}^r) \end{bmatrix} \begin{bmatrix} \partial_\theta u_{\theta(0)}(\mathbf{x}^b)^T & \partial_\theta \Phi[u_{\theta(0)}](\mathbf{x}^r)^T \end{bmatrix},$$

where Φ is the collection of all the partial derivatives of u , as in (4), and $\theta(0) \sim \mathcal{N}(0, \text{Id})$ i.i.d.. It follows that $K_\Phi(0)$ converges in probability to a deterministic limiting kernel as $m \rightarrow \infty$.

Proof. The component $\partial_\theta u_{\theta(0)}$ is linear, hence it is standard as in (Wang et al., 2022), Lemma 3.1. While the rest of the matrix needs to be generalized to any derivative Φ_i for $i = 1, \dots, k$.

For any $i, j = 1, \dots, k$ and every $x, x' \in \Omega$ consider each entry

$$\begin{aligned}
 \partial_\theta \Phi_i[u_{\theta(0)}](x) \partial_\theta \Phi_j[u_{\theta(0)}](x')^T &= \sum_{l=1}^{4m} \partial_{\theta_l} \Phi_i[u_{\theta(0)}](x) \partial_{\theta_l} \Phi_j[u_{\theta(0)}](x') \\
 &= \sum_{l=1}^{4m} \Phi_i[\partial_{\theta_l} u_{\theta(0)}](x) \Phi_j[\partial_{\theta_l} u_{\theta(0)}](x')
 \end{aligned}$$

where the second equality follows from Schwarz theorem (because of the smoothness of the derivatives of u), and the linearity of the operator Φ . This sum has to be split in 4 parts, one for each possible type of θ_l (in W^1, W^0, b^0 or b^1). Here we present the case when $\theta_l = W_l^1$, while the other cases are analogous:

$$\begin{aligned}
 \sum_{l=1}^m \Phi_i[\partial_{W_l^1} u_{\theta(0)}](x) \Phi_j[\partial_{W_l^1} u_{\theta(0)}](x') &= \frac{1}{m} \sum_{l=1}^m \Phi_i[\sigma(W_l^0(0)x + b_l^0(0))] \Phi_j[\sigma(W_l^0(0)x' + b_l^0(0))] \\
 &\xrightarrow{\mathcal{P}} \mathbb{E}_{u, v \sim \mathcal{N}(0,1)} [\Phi_i[\sigma(ux + v)] \Phi_j[\sigma(ux' + v)]],
 \end{aligned}$$

and the limit in probability in the last line comes from the law of Large Numbers. □

Lemma B.3. Suppose that there exist $R > 0$ and $\epsilon > 0$ such that $\forall \theta \in B(\theta(0), R)$ it holds

$$\begin{aligned}
 \|H_u(\mathbf{x}^b)\| &< \epsilon, \\
 \|H_{\Phi_j}(\mathbf{x}^b)\| &< \epsilon \quad \forall j = 1, \dots, k.
 \end{aligned}$$

Then $\max_{\theta \in B(\theta_0, R)} \|K_\Phi(t) - K_\Phi(0)\| = O(\epsilon R)$.

Proof. Using the properties of the spectral norm, we just need to bound each block of $J(t)$ as follows

$$\begin{aligned}
 \|J(t) - J(0)\| &\leq \sum_{i=0}^{N_r} \|\partial_\theta \Phi[u_{\theta(t)}](x_i^r) - \partial_\theta \Phi[u_{\theta(0)}](x_i^r)\| + \sum_{i=0}^{N_b} \|\partial_\theta u_{\theta(t)}(x_i^b) - \partial_\theta u_{\theta(0)}(x_i^b)\| \\
 &\leq kN_r \max_{i,j} \|\partial_\theta \Phi_j[u_{\theta(t)}](x_i^r) - \partial_\theta \Phi_j[u_{\theta(0)}](x_i^r)\| + N_b \max_i \|\partial_\theta u_{\theta(t)}(x_i^b) - \partial_\theta u_{\theta(0)}(x_i^b)\| \\
 &\leq kN_r \max_{i,j} \left(\max_{\theta \in B(\theta(0), R)} \|H_{\Phi_j}(x_i^r)\| \right) \|\theta - \theta_0\| + N_b \max_i \left(\max_{\theta \in B(\theta(0), R)} \|H_u(x_i^b)\| \right) \|\theta - \theta_0\| \\
 &\leq \max(kN_r, N_b) \epsilon R
 \end{aligned}$$

Hence:

$$\begin{aligned}
 \|K_\Phi(t) - K_\Phi(0)\| &= \|J(t)J(t)^T - J(0)J(0)^T\| \leq \|J(t) - J(0)\| \cdot (\|J(t)\| + \|J(0)\|) \\
 &\leq \max(kN_r, N_b) \epsilon R (\|J(t)\| + \|J(0)\|)
 \end{aligned}$$

and the last norm is bounded on $B(\theta(0), R)$ by smoothness of the model. \square

Lemma B.4. *Under Assumption 3.3 on the PDE and Assumption 3.4 on the network, then K_Φ is nearly constant during training, i.e.*

$$\lim_{m \rightarrow \infty} \sup_{t \in [0, T]} \|K_\Phi(t) - K_\Phi(0)\| = 0.$$

Proof. The statement follows by combining Lemma B.3 and Lemma D.1. \square

Now we are in position to prove Theorem 3.7:

Proof. (of Theorem 3.7) By using the chain rule on the residual term, we can explicitly compute:

$$\begin{aligned}
 K(0) &= \begin{bmatrix} \partial_\theta u_\theta(\mathbf{x}^b) \\ \partial_\theta r_\theta(\mathbf{x}^r) \end{bmatrix} \begin{bmatrix} \partial_\theta u_\theta(\mathbf{x}^b)^T & \partial_\theta r_\theta(\mathbf{x}^r)^T \end{bmatrix} = \\
 &= \begin{bmatrix} \partial_\theta u_\theta(\mathbf{x}^b) \\ \nabla R(\Phi[u_\theta](\mathbf{x}^r)) \partial_\theta \Phi[u_\theta](\mathbf{x}^r) \end{bmatrix} \begin{bmatrix} \partial_\theta u_\theta(\mathbf{x}^b)^T & \nabla R(\Phi[u_\theta](\mathbf{x}^r)) \partial_\theta \Phi[u_\theta](\mathbf{x}^r)^T \end{bmatrix} = \\
 &= \underbrace{\begin{bmatrix} \text{Id} & 0 \\ 0 & \nabla R(\Phi[u_\theta](\mathbf{x}^r)) \end{bmatrix}}_{\Lambda_R(0)} \underbrace{\begin{bmatrix} \partial_\theta u_\theta(\mathbf{x}^b) \\ \partial_\theta \Phi[u_\theta](\mathbf{x}^r) \end{bmatrix} \begin{bmatrix} \partial_\theta u_\theta(\mathbf{x}^b)^T & \partial_\theta \Phi[u_\theta](\mathbf{x}^r)^T \end{bmatrix}}_{K_\Phi(0)} \underbrace{\begin{bmatrix} \text{Id} & 0 \\ 0 & \nabla R(\Phi[u_\theta](\mathbf{x}^r))^T \end{bmatrix}}_{\Lambda_R(0)^T},
 \end{aligned}$$

where we have denoted $\theta(0)$ with θ and omitted the initial time step and $\nabla R(\Phi[u_\theta](\mathbf{x}^r))$ is defined in (16). Let us first observe that the linear part, i.e. $K_\Phi(0)$, converges in probability to a deterministic limit by Lemma B.2. Moreover, $\Phi[u_{\theta(0)}]$ converges in distribution to a gaussian process by Proposition B.1. Regarding the nonlinear part denoted with $\Lambda_R(0)$, we know by assumption that ∇R is a continuous function, hence we can apply the Continuous Mapping Theorem and conclude that

$$\nabla R(\Phi[u_\theta](x)) \xrightarrow{\mathcal{D}} \nabla R(\mathcal{GP}(0, \Sigma(x, x'))) \quad \text{for } x, x' \in \Omega.$$

From this, the convergence of $K(0)$ follows by Slutsky's theorem. \square

C. Proof of Proposition 3.9

Proof. Recall that we denote with $K(t)$ the NTK obtained with $\theta(t)$, evolving according to the gradient flow (7). Similarly, $K(0)$ is the NTK at initialization, i.e. with $\theta(0) \sim \mathcal{N}(0, \text{Id}_m)$. We can rewrite the kernels in terms of their linear and nonlinear part as we did for the proof of Theorem 3.7, and obtain

$$\begin{aligned}
 \lim_{m \rightarrow \infty} \sup_{t \in [0, T]} \|K(t) - K(0)\| &\geq \lim_{m \rightarrow \infty} \|K(t_m) - K(0)\| = \lim_{m \rightarrow \infty} \|\Lambda_R(t_m) K_\Phi(t_m) \Lambda_R(t_m)^T - \Lambda_R(0) K_\Phi(0) \Lambda_R(0)^T\| \\
 &\geq \lim_{m \rightarrow \infty} \left| \|\Lambda_R(t_m) K_\Phi(0) \Lambda_R(t_m)^T - \Lambda_R(0) K_\Phi(0) \Lambda_R(0)^T\| \right. \\
 &\quad \left. - \|\Lambda_R(t_m) [K_\Phi(t) - K_\Phi(0)] \Lambda_R(t_m)^T\| \right|,
 \end{aligned}$$

where the last is obtained by applying the inverse triangular inequality, after summing and subtracting the needed terms. Moreover, by considering that $\sup_{t \in [0, T]} \|K_\Phi(t) - K_\Phi(0)\| \rightarrow 0$ as $m \rightarrow \infty$ by Lemma B.4, we obtain that

$$\lim_{m \rightarrow \infty} \sup_{t \in [0, T]} \|K(t) - K(0)\| \geq \lim_{m \rightarrow \infty} \|\Lambda_R(t_m)K_\Phi(0)\Lambda_R(t_m)^T - \Lambda_R(0)K_\Phi(0)\Lambda_R(0)^T\| =$$

$$\lim_{m \rightarrow \infty} \left\| \begin{bmatrix} \text{Id} & 0 \\ 0 & \nabla R(\Phi[u(t_m)]) \end{bmatrix} K_\Phi(0) \begin{bmatrix} \text{Id} & 0 \\ 0 & \nabla R(\Phi[u(t_m)]) \end{bmatrix}^T - \begin{bmatrix} \text{Id} & 0 \\ 0 & \nabla R(\Phi[u_{\theta(0)}]) \end{bmatrix} K_\Phi(0) \begin{bmatrix} \text{Id} & 0 \\ 0 & \nabla R(\Phi[u_{\theta(0)}]) \end{bmatrix}^T \right\|.$$

Observe that (11) implies that $\Phi[u(t_m)] \rightarrow \Phi[u^*]$, hence $\nabla R(\Phi[u_{\theta(t)}]) \rightarrow \nabla R(\Phi[u^*])$ as $m \rightarrow \infty$ by continuity of ∇R . Combining this and Lemma B.2, we find

$$\lim_{m \rightarrow \infty} \left\| \begin{bmatrix} \text{Id} & 0 \\ 0 & \nabla R(\Phi[u(t_m)]) \end{bmatrix} K_\Phi(0) \begin{bmatrix} \text{Id} & 0 \\ 0 & \nabla R(\Phi[u(t_m)]) \end{bmatrix}^T - \begin{bmatrix} \text{Id} & 0 \\ 0 & \nabla R(\Phi[u_{\theta(0)}]) \end{bmatrix} K_\Phi(0) \begin{bmatrix} \text{Id} & 0 \\ 0 & \nabla R(\Phi[u_{\theta(0)}]) \end{bmatrix}^T \right\|$$

$$= \left\| \begin{bmatrix} \text{Id} & 0 \\ 0 & \nabla R(\Phi[u^*]) \end{bmatrix} K_\Phi(0) \begin{bmatrix} \text{Id} & 0 \\ 0 & \nabla R(\Phi[u^*]) \end{bmatrix}^T - \begin{bmatrix} \text{Id} & 0 \\ 0 & \nabla R(\Phi[u_{\theta(0)}]) \end{bmatrix} K_\Phi(0) \begin{bmatrix} \text{Id} & 0 \\ 0 & \nabla R(\Phi[u_{\theta(0)}]) \end{bmatrix}^T \right\|.$$

Finally, to prove our statement, we just need to show that the matrix above is not 0 almost surely, or at least one of its components. Let us fix a collocation point $x \in \Omega$ and let us define the function $f : \mathbb{R}^k \rightarrow \mathbb{R}$:

$$f(w) := \nabla R(\Phi[u^*](x))K_\Phi(0)_{(x,x)}\nabla R(\Phi[u^*](x))^T - \nabla R(w)K_\Phi(0)_{(x,x)}\nabla R(w)^T, \quad (18)$$

where $K_\Phi(0)_{(x,x)}$ denotes the kernel evaluation at a fixed collocation point. The first term on the right hand side of (18) is a deterministic vector, so f is a well defined deterministic analytic function. Moreover, if R is nonlinear, f is not identically zero.

By the properties of analytic functions we can conclude that $\text{Leb}(\{w \in \mathbb{R}^k | f(w) = 0\}) = 0$, where Leb denotes the Lebesgue measure. Notice that $\Phi[u_{\theta(0)}](x) \sim \mathcal{N}(0, \Sigma(x))$ in the infinite width limit as proven in Proposition B.1 and a consequence of that proof is that $\Sigma(x)$ is not singular. This implies that

$$\mathbb{P}(f(\Phi[u_{\theta(0)}](x)) = 0) = 0.$$

□

D. Proof of Proposition 3.11

We present here some preparatory results.

Lemma D.1. *For any $i = 1 \dots k$ and any $x \in \Omega$, the Hessian $H_{\Phi_i}(x)$ as defined in (17) is such that*

$$\|H_{\Phi_i}(x)\| = O\left(\frac{1}{\sqrt{m}}\right).$$

Proof. Recall that

$$(H_{\Phi_i}(x))_{jl} = \partial_{\theta_j \theta_l}^2 \Phi_i[u_\theta](x), \quad \text{where } l, j = 1, \dots, m.$$

By the linearity of the operator Φ_i and the smoothness of the activation function as in Assumption 3.4, it holds that

$$\partial_{\theta_j \theta_l}^2 \Phi_i[u_\theta] = \Phi_i \left[\partial_{\theta_j \theta_l}^2 u_\theta \right].$$

For a specific choice, e.g. first parameter is $\theta_j = W_j^1$ and the second is $\theta_l = W_l^0$, it holds that

$$\left| \partial_{W_j^1 W_l^0}^2 \Phi_i[u_\theta](x) \right| = \left| \Phi_i \left[\partial_{W_j^1 W_l^0}^2 u_\theta \right] \right| = \left| \frac{1}{\sqrt{m}} \Phi_i[\sigma'(W_l^0 x + b_l^0)x] \right| \mathbf{1}_{l=j} \leq C \frac{1}{\sqrt{m}}, \quad (19)$$

where the last inequality follow from Assumption 3.3, Assumption 3.4 and the boundedness of the domain Ω .

Since the calculations of (19) are similar for every combination of parameters W^1, W^0, b^0 , we do not report them here. Furthermore, we notice that the derivatives involving b^1 are zeros and hence we obtain that H_{Φ_i} is composed by 9 blocks

(3×3 combinations of parameters). Each block is a diagonal matrix, whose elements are bounded by $C \frac{1}{\sqrt{m}}$. By considering that the spectral norm of a diagonal matrix is equal to the maximum of its components, we can bound the spectral norm of each block by $C \frac{1}{\sqrt{m}}$. Moreover the spectral norm of a matrix can be bounded by the sum of the spectral norm of its blocks, hence:

$$\|H_{\Phi_i}(x)\| \leq 9C \frac{1}{\sqrt{m}} = O\left(\frac{1}{\sqrt{m}}\right).$$

□

We can now prove Proposition 3.11.

Proof. In the nonlinear case the Hessian of the residuals is

$$\begin{aligned} (H_r(x))_{j,l} &= \partial_{\theta_l}^2 r_\theta(x) = \partial_{\theta_l} (\nabla R(\Phi[u_\theta](x))) \partial_{\theta_j} u_\theta(x) = \\ &= \underbrace{\langle \partial_{\theta_l} \Phi[u_\theta](x), \nabla^2 R(\Phi[u_\theta](x)) \partial_{\theta_j} \Phi[u_\theta](x) \rangle}_{A_{ij}} + \underbrace{\nabla R(\Phi[u_\theta](x)) H_\Phi(x)}_{B_{ij}}. \end{aligned}$$

for every collocation point $x \in \Omega$. The matrix H_Φ is defined in (17). Moreover, Lemma D.1 provides that the spectral norm of B goes to 0 in the infinite width limit. Moreover, by making use of the inverse triangular inequality, we obtain that for any $x \in \Omega$, it holds

$$\lim_{m \rightarrow \infty} \|H_r(x)\| \geq \lim_{m \rightarrow \infty} \|\|A\| - \|B\|\| = \lim_{m \rightarrow \infty} \|A\|.$$

According to the definition of spectral norm, we have that

$$\lim_{m \rightarrow \infty} \|A\| = \lim_{m \rightarrow \infty} \max_{\|z\|_2 \leq 1} \|Az\|_2 \geq \lim_{m \rightarrow \infty} \|A\bar{z}\|_2,$$

where $\bar{z} := \left[\frac{1}{\sqrt{m}} \quad \frac{1}{\sqrt{m}} \quad \dots \quad \frac{1}{\sqrt{m}} \right]$. Let us now focus on the term $\|A\bar{z}\|_2$. By using some standard inequalities and taking advantage of the fact that each entry of \bar{z} is $\frac{1}{\sqrt{m}}$, we obtain that

$$\begin{aligned} \|Az\|_2 &\geq \frac{1}{\sqrt{m}} \|Az\|_1 \geq \frac{1}{\sqrt{m}} \sum_{i=1}^m (Az)_i = \frac{1}{m} \sum_{i,j=1}^m A_{ij} \\ &= \frac{1}{m} \sum_{i,j=1}^m \langle \partial_{\theta_i} \Phi[u_\theta](x), \nabla^2 R(\Phi[u_\theta](x)) \partial_{\theta_j} \Phi[u_\theta](x) \rangle = \\ &= \left\langle \frac{1}{\sqrt{m}} \sum_{i=1}^m \partial_{\theta_i} \Phi[u_\theta](x), \nabla^2 R(\Phi[u_\theta](x)) \frac{1}{\sqrt{m}} \sum_{j=1}^m \partial_{\theta_j} \Phi[u_\theta](x) \right\rangle \end{aligned}$$

Without loss of generality, we can restrict our focus to $\theta_i = W_i^1$ and $\theta_j = W_j^1$, since the spectral norm of a matrix is greater or equal then the norm of its submatrix, and study the term

$$\lim_{m \rightarrow \infty} \frac{1}{\sqrt{m}} \sum_{i=1}^m \partial_{\theta_i} \Phi[u_\theta](x) = \lim_{m \rightarrow \infty} \frac{1}{m} \sum_{i=1}^m \Phi[\sigma(W_i^0 \cdot + b_i^0)](x) = \mathbb{E}_{u, v \sim \mathcal{N}(0,1)} [\Phi[\sigma(u \cdot + v)](x)] =: w \quad (20)$$

by the law of large numbers. In particular, w is deterministic. Notice that here we have considered a generic θ since, according to Lemma B.4, $\partial_{\theta_i} \Phi$ is constant. By combining this result with the previous one, we obtain that

$$\lim_{m \rightarrow \infty} \|H_r(x)\| \geq w^T \nabla^2 R(\Phi[u_\theta](x)) w \geq \tilde{c}$$

where \tilde{c} is a deterministic constant that does not depend on m , but only on the value of $\nabla^2 R$ (which is constant because R is a second-order polynomial) and on the vector w defined in (20). □

E. Proof of Theorem 4.3

Proof. The gradient flow equation in case of Gauss-Newton methods has been defined in (14) for $J(t) \in \mathbb{R}^{n \times p}$ where $t \in [0, T]$. It follows that

$$\begin{bmatrix} \partial_t u_{\theta(t)} \\ \partial_t r_{\theta(t)} \end{bmatrix} = \begin{bmatrix} \partial_{\theta} u_{\theta(t)} \\ \partial_{\theta} r_{\theta(t)} \end{bmatrix} \partial_t \theta(t) = J(t) \partial_t \theta(t) = -J(t)(J^T(t)J(t))^\dagger J^T \begin{bmatrix} u_{\theta(t)} \\ r_{\theta(t)} \end{bmatrix},$$

where the last equality comes from plugging in (14) into the equation. Now, let us consider the case when $p \gg n$, then the singular value decomposition of $J(t)$ is as follows

$$J(t) = U \underbrace{\begin{bmatrix} \tilde{\Sigma}_n & 0_{p-n} \end{bmatrix}}_{\Sigma} V^T,$$

where $U \in \mathbb{R}^{n \times n}$, $\Sigma \in \mathbb{R}^{n \times p}$, $V \in \mathbb{R}^{p \times p}$ and $\tilde{\Sigma}_n \in \mathbb{R}^{n \times n}$ is a diagonal matrix with elements given by the square roots of the eigenvalues of the NTK. We drop the dependence on time t of U , Σ and V to ease the notation. Let us now study the term

$$\begin{aligned} J(t)(J^T(t)J(t))^\dagger J^T(t) &= U \Sigma^T V^T (V \Sigma^T U^T U \Sigma V^T)^\dagger V \Sigma^T U^T \\ &= U \Sigma V^T V (\Sigma^T \Sigma)^\dagger V^T V \Sigma^T U^T \\ &= U \Sigma (\Sigma^T \Sigma)^\dagger \Sigma^T U^T \\ &= U \begin{bmatrix} \tilde{\Sigma}_n & 0_{p-n} \end{bmatrix} \left(\begin{bmatrix} \tilde{\Sigma}_n \\ 0_{p-n} \end{bmatrix} \begin{bmatrix} \tilde{\Sigma}_n & 0_{p-n} \end{bmatrix} \right)^\dagger \begin{bmatrix} \tilde{\Sigma}_n \\ 0_{p-n} \end{bmatrix} U^T \\ &= U \begin{bmatrix} \tilde{\Sigma}_n & 0_{p-n} \end{bmatrix} \begin{bmatrix} \tilde{\Sigma}_n^2 & 0_{p-n} \\ 0_{p-n} & 0_n \end{bmatrix}^\dagger \begin{bmatrix} \tilde{\Sigma}_n \\ 0_{p-n} \end{bmatrix} U^T \\ &= U \tilde{\Sigma}_n (\tilde{\Sigma}_n^2)^\dagger \tilde{\Sigma}_n U^T \\ &= U D U^T \end{aligned}$$

where D is obtained from $\tilde{\Sigma}_n$ by replacing the non-zero components with 1. In particular we can rewrite the Gauss-Newton flow as:

$$\begin{bmatrix} \partial_t u_{\theta(t)} \\ \partial_t r_{\theta(t)} \end{bmatrix} = -U D U^T \begin{bmatrix} u_{\theta(t)} \\ r_{\theta(t)} \end{bmatrix}.$$

Notice that it has the same form of the gradient flow in Lemma 3.2 but the Neural Tangent Kernel is replaced by a matrix with non-zero eigenvalues 1. This can be translated as: second-order optimizers are almost spectrally unbiased. Moreover if $J(t)$ stays full rank during the training, we can obtain the result of convergence regardless of the singular values of $J(t)$, i.e.:

$$\begin{bmatrix} \partial_t u_{\theta(t)} \\ \partial_t r_{\theta(t)} \end{bmatrix} = - \begin{bmatrix} u_{\theta(t)} \\ r_{\theta(t)} \end{bmatrix}.$$

□

F. Details about the Numerical Experiments

F.1. The LM Algorithm

In the following, we provide a more detailed description of the version of the Levenberg-Marquardt algorithm along with its pseudocode and the details of the experiments whose results are shown in Section 5.

The main difference between the Levenberg-Marquardt algorithm and other Quasi-Newton methods is that general Quasi-Newton methods are line-search approaches, while LM is a trust region approach. In practice, line search approaches determine a descent direction of the loss function and thereafter determine a suitable step size in such direction. On the other hand, a trust region method determines an area where the solution lies and computes the optimal step. If this step does not provide enough improvement in the objective function, the search area is reduced and the search is performed once more. We refer to (Nocedal & Wright, 1999) for a thorough description of trust region and line search methods.

In the following part, we drop the dependence on training time as a continuous function and identify $f(t_k) = f_k$ for some discrete time t_k . As already mentioned in Section 5, the update step v_k of the LM algorithm is computed follows:

$$v_k = - [J_k^T J_k + \lambda D_k]^{-1} \nabla L(\theta_k). \quad (21)$$

Where D_k is a diagonal matrix of size $n \times n$. In the classical LM algorithm, this matrix D_k is given by the identity matrix. Another viable alternative recommended in (Fletcher, 1971) is to use the diagonal of $J_k^T J_k$. For our model, we choose D_k to be simply the identity matrix, which appears to be more stable when $J_k^T J_k$ is singular.

Another typical modification to the Levenberg-Marquardt algorithm is the introduction of the geodesic acceleration (Transtrum & Sethna, 2012).

$$a_k = - [J_k^T J_k + \lambda D_k]^{-1} v_k H_r v_k. \quad (22)$$

The goal of the geodesic acceleration is to introduce a component which does consider all the components of the Hessian of the loss when the residuals are not small and when the Hessian of the residuals is not negligible.

Moreover, at every iteration, one has to specify a criterion C_k whose objective is to evaluate the relative improvement of the model parameterized by θ_k with respect to the update step v_k . The criterion depends on the modification of the LM algorithm chosen. For our algorithm we use the same condition as (Gavin, 2019) i.e. $C_k < toll$ where C_k is defined as

$$C_k = \frac{L(\theta_k)^2 - L(\theta_k + v_k)^2}{\langle v_k, \lambda_k D_k v_k + \nabla L(\theta_k) \rangle}. \quad (23)$$

We provide in Algorithm 1 the pseudocode of the modified LM algorithm that we chose for our numerical experiments, inspired by the implementation of (Gavin, 2019) and modifying it by adding the component of the geodesic acceleration.

Algorithm 1 Modified Levenberg-Marquardt Algorithm

Input: Maximum region area $\Lambda > 0$, Region Radius $0 < \lambda_0 < \Lambda$, Tolerance $toll \in [0, \frac{1}{4})$, $\alpha \in [0, 1)$

for $k = 0, 1, 2, \dots$ **do**

 Compute v_k as in Equation (21)

 Compute criterion C_k as in Equation (23)

while $C_k < toll$ **do**

$\lambda = \min(2\lambda, \Lambda)$

 Compute v_k with the new value of λ

 Compute criterion C_k as in Equation (23)

end while

$\theta_{k+1} = \theta_k + v_k$

$\lambda_{k+1} = \max(\frac{1}{3}\lambda, \Lambda^{-1})$

 Compute a_k as in Equation (22)

if $2\|a_k\| \leq \alpha\|v_k\|$ **then**

$\theta_{k+1} = \theta_{k+1} + \frac{1}{2}a_k$

end if

end for

The main focus of the Levenberg-Marquardt method is to decide the size of the trust region. In practice, at every iteration, one wants to find a better solution and afterwards reduce the size of the trust region. When this does not happen, the solution is to enlarge the trust region in order to look for a better solution. In our method we choose to include the region search as part of the inner loop, as for line search approaches. This means that the iteration itself can be slower, but more accurate, which is why we include in the numerical evaluation also the computational time.

F.2. Poisson Equation

The Poisson equation that we choose for our study is a monodimensional instance of the PDE defined in (Wang et al., 2021b) for $x \in \Omega = [0, 1]$ and we try to find the solution $u : \Omega \rightarrow \mathbb{R}$. In particular, we want to solve the following equation:

$$\begin{aligned} \partial_x^2 u &= f(x), & x \in \Omega, \\ u(0) &= u(1) = 0. \end{aligned} \quad (24)$$

As in (Wang et al., 2021b), the function f is constructed in such a way that the exact solution of Equation (24) is given by:

$$u(x) = \sin(2\pi x) + \frac{1}{10} \sin(50\pi x).$$

This approach is done to evaluate the behavior of PINNs when the target solution presents a high frequency and a low frequency component. We then train the PINN model by sampling $N_r = 10^3$ points in Ω with latin hypercube sampling.

F.3. Wave Equation

We opt to solve the wave equation below for each $(x, \tau) \in \Omega = [0, 1]^2$ and aim to find the solution $u : \Omega \rightarrow \mathbb{R}$. In particular, we aim to solve the following equation:

$$\begin{aligned} \partial_\tau^2 u &= -C^2 \partial_x^2 u, & (x, \tau) \in \Omega, \\ u(x, 0) &= \sin(\pi x) + \frac{1}{2} \sin(4\pi x), & x \in [0, 1], \\ \partial_\tau u(x, 0) &= 0 & x \in [0, 1], \\ u(0, \tau) &= u(1, \tau) = 0, & \tau \in [0, 1]. \end{aligned} \tag{25}$$

With C being equal to 2 for our case. It is straightforward to obtain the correct solution of this equation through Fourier transform. In particular, the exact solution of Equation (25) is given by:

$$u(x, \tau) = \sin(\pi x) \cos(2\pi\tau) + \frac{1}{2} \sin(4\pi x) \cos(8\pi\tau).$$

We then train a PINN by sampling $N_r = 10^4$ training points in Ω for the PDE residuals with latin hypercube sampling, and $N_b = 3 \cdot 10^3$ points for training the model against the correct solution at $\partial\Omega$.

F.4. Burger Equation

Burger equation is a 1D version of Navier-Stokes equations. Its solution at high times present a discontinuity, which makes it challenging for spectrally biased architectures. The specific instance chosen in our numerics for Burger equation is the same as in (Raissi, 2018). In particular, we refer to the exact same data for provided by the authors. In particular, given $(x, \tau) \in \Omega = [-1, 1] \times [0, 1]$, we solve for $u : \Omega \rightarrow \mathbb{R}$ the following equation:

$$\begin{aligned} \partial_\tau u + u \partial_x u - \nu \partial_x^2 u &= 0, & (x, \tau) \in \Omega, \\ u(x, 0) &= -\sin(\pi x), & x \in [-1, 1], \\ u(-1, \tau) &= u(1, \tau) = 0, & \tau \in [0, 1], \end{aligned} \tag{26}$$

with the diffusivity ν being equal to $\frac{0.01}{\pi}$ for this specific instance. The correct solution is provided publicly by the authors of (Raissi, 2018).

Training is performed with $N_r = 10^4$ collocation points for training the PDE residuals, sampled with latin hypercube sampling, and $N_b = 3 \cdot 10^3$ points for training the boundary and initial condition in $\partial\Omega$.

F.5. Navier-Stokes Equation

The most interesting scenario taken in consideration for our experiments is that of Navier-Stokes equations. In particular, we aim to solve the fluid flow past a cylinder in 2D tackled in (Raissi et al., 2020). In particular, we have $(x, y, t) \in \Omega = [-2.5, 7.5] \times [-2.5, 2.5] \times [0, 7]$ and we wish to find $\vec{u} : \Omega \rightarrow \mathbb{R}^3$ which is defined as $\vec{u}(x, y, t) = [u(x, y, t), v(x, y, t), p(x, y, t)]^T$. In particular u and v are respectively the horizontal and vertical components of the fluid velocity and p is the pressure at a point. Navier-Stokes equations are then expressed in vectorizer form

as follows:

$$\begin{aligned}
 \partial_\tau u + u\partial_x u + v\partial_y u - \frac{1}{Re}(\partial_x^2 u + \partial_y^2 u) + \partial_x p &= 0, & (x, y, \tau) \in \Omega, \\
 \partial_\tau v + u\partial_x v + v\partial_y v - \frac{1}{Re}(\partial_x^2 v + \partial_y^2 v) + \partial_y p &= 0, & (x, y, \tau) \in \Omega, \\
 \partial_x u + \partial_y v &= 0, & (x, y, \tau) \in \Omega, \\
 u(x, y, 0) = g_{u_0}(x, y), & & (x, y) \in [-2.5, 7.5] \times [-2.5, 2.5], \\
 v(x, y, 0) = g_{v_0}(x, y), & & (x, y) \in [-2.5, 7.5] \times [-2.5, 2.5], \\
 u(-2.5, y, \tau) = 1, & & (y, \tau) \in [-2.5, 2.5] \times [0, 7], \\
 v(-2.5, y, \tau) = 0, & & (y, \tau) \in [-2.5, 2.5] \times [0, 7],
 \end{aligned} \tag{27}$$

where Re represents the Reynolds' number, which is an adimensional quantity defined by the problem and is set to 100 for our case. The initial conditions (g_{u_0}, g_{v_0}) can be found in the repository published by the authors of (Raissi et al., 2020), as well as the correct solution. The conditions at $x = -2.5$ represents the fluid velocity imposed at the inlet, and further conditions are given by the presence of a cylinder centered in $(x, y) = (0, 0)$ with radius 0.25. Furthermore, an additional condition appears at the borders, namely where $y = \pm 2.5$, where the no-slip condition can be chosen ($u = v = 0$) or the correct solution can be given as boundary condition. Since the simulation provided in (Raissi et al., 2020) refers to a free-flow stream, we use the correct solution at the boundaries.

To train our PINNs, we use $N_r = 5 \cdot 10^5$ collocation points for training the PDE residuals, sampled with latin hypercube sampling, and $N_b = 2 \cdot 10^4$ points for training the boundary and initial condition in $\partial\Omega$. Moreover, at every iteration, we minimize the loss on random batches of the training data, respectively 10^4 points for the residuals and $5 \cdot 10^3$ for boundary and initial condition.